Supplementary material to: Non-local signatures of the chiral magnetic effect in Dirac semimetal $Bi_{0.97}Sb_{0.03}$

Jorrit C. de Boer,[1,*] Daan H. Wielens,[1,*] Joris A. Voerman,[1] Bob de Ronde,[1] Yingkai Huang,[2] Mark S. Golden,[2] Chuan Li,[1] and Alexander Brinkman[1]

[1] *MESA$^+$ Institute for Nanotechnology, University of Twente, The Netherlands*
[2] *Van der Waals - Zeeman Institute, IoP, University of Amsterdam, The Netherlands*

APPENDIX A: EFFECTIVE HAMILTONIAN AND THE CHIRAL MAGNETIC EFFECT

A1. Cd_3As_2

Cd_3As_2 is a Dirac semimetal belonging to the point group D_{4h}. The 2-fold inversion symmetry in this system ensures two topologically protected Dirac points along the k_z-axis. To explore the electronic structure of Cd_3As_2 we utilize a linearized version of the $k\cdot p$ model Hamiltonian as defined by B.J. Yang and Nagaosa [1]:

$$H_{\text{eff}} = v_{\parallel}(k_x\,\sigma_x s_z + k_y\,\sigma_y s_0) \pm v_z\,k_z\,\sigma_z s_0, \qquad (1)$$

where $\pm$ is used to switch between the nodes residing at $k_z' = \pm k_D$ and k_z is measured relative to the center of the node. The total angular momentum and orbital degrees of freedom are indicated by s and σ, respectively. We can see that Cd_3As_2 exhibits orbital-momentum locking and is of the form $(\boldsymbol{k}\cdot\boldsymbol{\sigma})s_0$. Assuming isotropic spin-orbit coupling strength ($v_{\parallel} = v_z = v_F$) and switching to spherical coordinates with θ the angle in the xy-plane and φ the polar angle measured from $+k_z$, we get

$$H_{\text{eff}} = \hbar v_F \begin{bmatrix} \pm\cos\varphi & \sin\varphi\, e^{i\theta} & 0 & 0 \\ \sin\varphi\, e^{-i\theta} & \mp\cos\varphi & 0 & 0 \\ 0 & 0 & \pm\cos\varphi & -\sin\varphi\, e^{-i\theta} \\ 0 & 0 & -\sin\varphi\, e^{i\theta} & \mp\cos\varphi \end{bmatrix}, \qquad (2)$$

where the basis is taken as $\{|s\uparrow\rangle, |p_x + ip_y\uparrow\rangle, |s\downarrow\rangle, |p_x - ip_y\downarrow\rangle\}$. In this case, the eigenenergies are simply $E_{\pm} = \pm v_F\boldsymbol{k}$. For a system doped to the n-type regime so that $E > 0$, we can find the normalized spinors at the $k_z = -k_D$ Dirac point, which we will refer to as node 1:

$$\begin{aligned} \psi^1_+(\boldsymbol{k}) &= \left(e^{i\theta}\cos\varphi/2,\, \sin\varphi/2,\, 0,\, 0\right)^T \\ \psi^1_-(\boldsymbol{k}) &= \left(0,\, 0,\, -e^{-i\theta}\cos\varphi/2,\, \sin\varphi/2\right)^T. \end{aligned} \qquad (3)$$

For node 2, located at $k_z = +k_D$, we have

$$\begin{aligned} \psi^2_+(\boldsymbol{k}) &= \left(\sin\varphi/2\, e^{i\theta},\, \cos\varphi/2,\, 0,\, 0\right)^T \\ \psi^2_-(\boldsymbol{k}) &= \left(0,\, 0,\, -\sin\varphi/2\, e^{i\theta},\, \cos\varphi/2\right)^T. \end{aligned} \qquad (4)$$

To find the topological properties of node 1, we first need to find the Berry connection $A^1_+ = i\langle\psi^1_+(\boldsymbol{k})|\nabla_k\psi^1_+(\boldsymbol{k})\rangle$. Because in spherical coordinates $\nabla_k = \frac{\partial}{\partial k}\hat{k} + \frac{1}{k}\frac{\partial}{\partial\varphi}\hat{\varphi} + \frac{1}{k\sin\varphi}\frac{\partial}{\partial\theta}\hat{\theta}$, we get

$$A^1_+ = -\frac{\cos^2\varphi/2}{k\,\sin\varphi}\hat{\theta}. \qquad (5)$$

From this, we find that the Berry curvature

$$\Omega^1_+ = \nabla\times A^1_+ = \frac{1}{k\sin\varphi}\frac{\partial}{\partial\varphi}(A^1_+\sin\varphi)\hat{k} = \frac{1}{2k^2}\hat{k}. \qquad (6)$$

This Berry curvature can be seen as a magnetic field in k-space and indicates the monopole character of the node. The flux coming from each node gives us, once normalized by 2π, the "chirality" or "Chern number" of the node:

$$\chi^1_+ = \frac{1}{2\pi}\int_0^{2\pi}\int_0^{\pi}\Omega^1_+\,k^2\sin\varphi\;d\varphi\,d\theta = 1. \qquad (7)$$

Similarly, we find $\chi^1_- = -1$ and for node 2 we find $\chi^2_+ = -1$ and $\chi^2_- = +1$. First of all, this shows us that the Dirac points in this material have Chern number ±1, which makes Cd_3As_2 topological. Furthermore, it seems that the degenerate Dirac cones have opposite chirality, and that the nodes at $k_z \to \mp k_D$ also have opposite chiralities (figure 1(a)), reflecting the 2-fold inversion symmetry of the system.

As the k-space analogue, the Berry curvature also has to be taken into account in the equations of motion that describe the equilibrium state of the system. Since the chiralities tell us that some Dirac points act as sources of Berry curvature and others as drains, the signs of the forces due to the Berry curvature are also opposite. This results in a net imbalance between cones of opposite chirality, a so called "chiral charge imbalance". In this section, we will derive the resulting charge pumping by studying the Landau levels.

As Eqn. (2) consists of 2 decoupled Weyl cones of the form $H = \pm v_F\boldsymbol{\sigma}\cdot\boldsymbol{p}$, where $\boldsymbol{\sigma}$ denotes the orbital degree of freedom, one can easily find the Landau level dispersion relations as described by Zyuzin *et al.* [2]. In short, one includes the vector potential correction to the momentum as $\boldsymbol{\pi} = \boldsymbol{p} + e\boldsymbol{A}$ and rewrites the Hamiltonian in terms of $a = (\pi_x - i\pi_y)/\sqrt{2\hbar eB}$ and $a^\dagger = (\pi_x + i\pi_y)/\sqrt{2\hbar eB}$ (for a magnetic field $\boldsymbol{B} = B_z$):

$$\begin{aligned} H &= \pm\hbar\omega(\sigma_+ a + \sigma_- a^\dagger) \pm \hbar v_F\sigma_z k_z \\ H &= \pm\begin{bmatrix} \hbar v_F k_z & \hbar\omega a \\ \hbar\omega a^\dagger & -\hbar v_F k_z \end{bmatrix}, \end{aligned} \qquad (8)$$

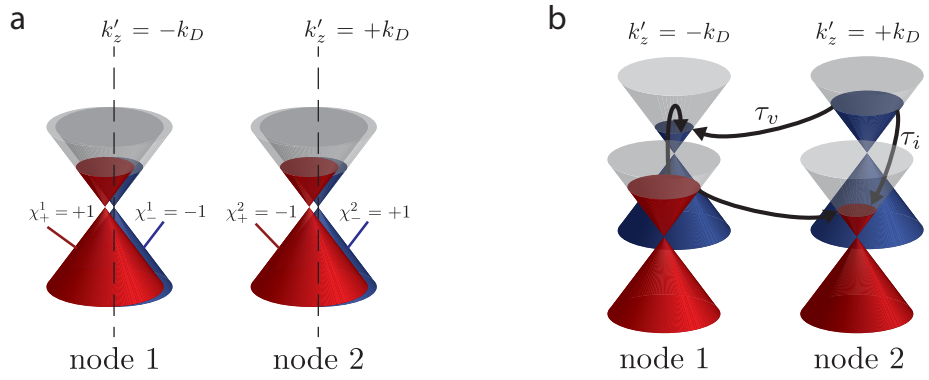

FIG. 1: **Schematic of the Cd_3As_2 band structure.** **(a)** Cd_3As_2 has 2 nodes (or 'valleys') on the k_z-axis, each 2-fold degenerate ($\chi = \pm 1$). In valley 2, the chiralities are opposite to those in valley 1. **(b)** The chiral magnetic effect causes charge pumping from Fermi surfaces with $\chi = -1$ to those with $\chi = +1$. At a certain charge pumping rate, the 'chiral charge imbalance' is equilibrated by intercone relaxation processes, which can be intervalley or isospin-flip processes. For clarity, the degenerate cones of different isospin were given an offset in panel (b).

where $\sigma_\pm = (\sigma_x \pm i\sigma_y)/2$. Assuming a wavefunction of the form $\psi_n = (u_n|n-1\rangle, v_n|n\rangle)^T$, the creation and annihilation operators can be replaced according to $a|n\rangle = \sqrt{n}|n-1\rangle$ and $a^\dagger|n-1\rangle = \sqrt{n}|n\rangle$. To find the dispersion relation one can solve $\det(H - \sigma_0 E_n) = 0$ with

$$H = \begin{bmatrix} \hbar v_F k_z & \hbar\omega\sqrt{n} \\ \hbar\omega\sqrt{n} & -\hbar v_F k_z \end{bmatrix} \tag{9}$$

to find $E_n = \pm\hbar\omega\sqrt{n + (v_F k_z/\omega)^2}$. Here, $\pm$ corresponds to the chirality of the accompanying wavefunction, as shown in Eqn. 7. For $n = 0$, this gives us the dispersion of the zeroth Landau level: $E_0 = \pm\hbar v_F k_z$, which describes a linear dispersion with a Fermi velocity parallel or anti-parallel to $\boldsymbol{B} = B_z$, depending on the chirality of the Weyl node. It can be shown in a rather easy way that a dispersion relation of this form leads to a chiral charge imbalance [2]. The resulting charge pumping between Dirac cones of opposite chirality is balanced by relaxation processes (see figure 1(b)). Orthogonality of isospin and the large $\Delta\boldsymbol{k}$ involved with intervalley scattering significantly increase the relaxation times (τ_i and τ_v respectively), so that the chiral charge imbalance becomes a relevant quantity in transport measurements.

A2. $Bi_{1-x}Sb_x$

$Bi_{1-x}Sb_x$ belongs to the point group D_{3D} and has 3-fold rotation symmetry. There are no symmetries in this system that ensure the presence of Dirac cones, and the Dirac cones that do reside at the L-points are therefore labelled as accidental band touchings. Due to the 3-fold rotation symmetry, $Bi_{1-x}Sb_x$ has three accidental Dirac cones, separated by 120°. Topological Bi compounds can generally be described using the model Hamiltonian for topological insulators as developed by Liu *et al.* [3]. Assuming isotropic Fermi velocities and taking $m \to 0$, the linearized Hamiltonian can be written as

$$H_{\text{Liu}} = \hbar v_F \sigma_x (s_x k_y - s_y k_x) + \hbar v_F \sigma_y s_0 k_z. \tag{10}$$

Teo *et al.* [4] described the Dirac physics around a single L-point in $Bi_{1-x}Sb_x$ in great detail using a modified form of this Hamiltonian, which can be obtained as $H_{\text{TFK}} = U_{\text{R}}^\dagger H_{\text{Liu}} U_{\text{R}}$ with $U_{\text{R}} = (s_0 - is_x - is_y - is_z)/2$ (a $-2\pi/3$ rotation along the [111]-axis in spin space) and taking $v_x \to -v_x$:

$$H_{\text{TFK}} = \hbar v_F \sigma_x (s_x k_x + s_z k_y) + \hbar v_F \sigma_y s_0\, k_z. \tag{11}$$

The spinor part of the two wavefunctions for the conduction band side of the cone can be written as

$$\begin{aligned} \psi_+(\boldsymbol{k}) &= \frac{1}{\sqrt{2}}\big(\cos\varphi/2, -e^{i\theta}\sin\varphi/2, e^{i\theta}\sin\varphi/2, \cos\varphi/2\big)^T \\ \psi_-(\boldsymbol{k}) &= \frac{1}{\sqrt{2}}\big(\sin\varphi/2, e^{i\theta}\cos\varphi/2, e^{i\theta}\cos\varphi/2, -\sin\varphi/2\big)^T. \end{aligned} \tag{12}$$

In the same manner as for Cd_3As_2, we can use these spinors to find the Berry curvature $\Omega^1_+ = \nabla \times A_\pm = \pm\frac{1}{2k^2}\hat{k}$ and the chirality $\chi_\pm = \pm 1$. The unitary transformation U_{R} can be used to transform ψ_{TFK} into ψ_{Liu}, so that the topological properties of H_{Liu} are the same as those found for H_{TFK}. To find out of this leads to the chiral magnetic effect in $Bi_{1-x}Sb_x$, we consider the full 4x4 Hamiltonian.

For a magnetic field along the c-axis we use H_{Liu}, with the spin space rotated by 90° along the s_z-axis so that, in the basis $\{|\sigma_1\uparrow\rangle, |\sigma_1\downarrow\rangle, |\sigma_2\uparrow\rangle, |\sigma_2\downarrow\rangle\}$, the effective

Hamiltonian takes the form:

$$H'_{\rm Liu} = \hbar v_F \sigma_x (s_x k_x + s_y k_y) + \hbar v_F \sigma_y s_0 \, k_z = \hbar v_F \begin{bmatrix} 0 & 0 & -ik_z & k_x - ik_y \\ 0 & 0 & k_x + ik_y & -ik_z \\ ik_z & k_x - ik_y & 0 & 0 \\ k_x + ik_y & ik_z & 0 & 0 \end{bmatrix}. \quad (13)$$

The orbital shift due to the vector potential is included as $\boldsymbol{\pi} = \boldsymbol{p} + e\boldsymbol{A}$, which we write again as creation and annihilation operators: $a = (\pi_x - i\pi_y)/\sqrt{2\hbar eB}$ and $a^\dagger = (\pi_x + i\pi_y)/\sqrt{2\hbar eB}$. The corresponding raising and lowering matrices are $s_\pm = \sigma_x(s_x \pm i s_y)$. Then

$$H'_{\rm Liu} = \begin{bmatrix} 0 & 0 & -i\hbar v_F k_z & \hbar\omega a \\ 0 & 0 & \hbar\omega a^\dagger & -i\hbar v_F k_z \\ i\hbar v_F k_z & \hbar\omega a & 0 & 0 \\ \hbar\omega a^\dagger & i\hbar v_F k_z & 0 & 0 \end{bmatrix}, \quad (14)$$

where $\hbar\omega = v\sqrt{2\hbar eB}$. As a trial wavefunction, we double the basis used for the 2x2 case: $\psi_n = (u_n^1|n-1\rangle, v_n^1|n\rangle, u_n^2|n-1\rangle, v_n^2|n\rangle)^T$. To find the dispersion relations for this wavefunction, we solve

$$\det \begin{bmatrix} -E_n & 0 & -i\hbar v_F k_z & \hbar\omega\sqrt{n} \\ 0 & -E_n & \hbar\omega\sqrt{n} & -i\hbar v_F k_z \\ i\hbar v_F k_z & \hbar\omega\sqrt{n} & -E_n & 0 \\ \hbar\omega\sqrt{n} & i\hbar v_F k_z & 0 & -E_n \end{bmatrix} = 0. \quad (15)$$

This gives us $E_n = \pm\hbar\omega\sqrt{n + (v_F k_z/\omega)^2}$, exactly the same result as we found for Cd_3As_2, including the linear zeroth Landau levels.

The simplified Cd_3As_2 Hamiltonian we employed earlier has isotropic orbital-momentum locking $\hbar v_F \boldsymbol{\sigma}\cdot\boldsymbol{k}$, so that the Landau level formation is the same for magnetic fields in all directions. $H'_{\rm Liu} = \hbar v_F \sigma_x (s_x k_x + s_y k_y) + \hbar v_F \sigma_y s_0 \, k_z$ has a clear difference between the spin-momentum locking in the in-plane k_x and k_y directions, and the k_z direction, so a different response to magnetic field from different directions can be expected. To study the effect of a magnetic field along the k_x-axis (B_x), we first perform a rotation along the [111]-axis in spin space ($U_{\rm R} = (s_0 - is_x - is_y - is_z)/2$) to get:

$$H''_{\rm Liu} = U_{\rm R} H'_{\rm Liu} U_{\rm R}^\dagger = \hbar v_F \sigma_x (s_y k_x + s_z k_y) + \hbar v_F \sigma_y s_0 \, k_z = \hbar v_F \begin{bmatrix} 0 & 0 & ky - ik_z & -ik_x \\ 0 & 0 & ik_x & -(ky + ik_z) \\ ky + ik_z & -ik_x & 0 & 0 \\ ik_x & -(ky - ik_z) & 0 & 0 \end{bmatrix}, \quad (16)$$

which makes the following operations easier. With the modified raising and lowering matrices $s_\pm = \sigma_x s_z \pm i\sigma_y s_0$) and operators $a = (\pi_y - i\pi_z)/\sqrt{2\hbar eB}$ and $a^\dagger = (\pi_y + i\pi_z)/\sqrt{2\hbar eB}$, we can rewrite $H''_{\rm Liu}$ into

$$H''_{Liu} = \begin{bmatrix} 0 & 0 & \hbar\omega a & -i\hbar v_F k_x \\ 0 & 0 & i\hbar v_F k_x & -\hbar\omega a^\dagger \\ \hbar\omega a^\dagger & -i\hbar v_F k_x & 0 & 0 \\ i\hbar v_F k_x & -\hbar\omega a & 0 & 0 \end{bmatrix}. \quad (17)$$

With $\psi_n = (u_n^1|n-1\rangle, v_n^1|n\rangle, v_n^2|n\rangle, u_n^2|n-1\rangle)^T$, we find from

$$\det \begin{bmatrix} -E_n & 0 & \hbar\omega\sqrt{n} & -i\hbar v_F k_x \\ 0 & -E_n & i\hbar v_F k_x & -\hbar\omega\sqrt{n} \\ \hbar\omega\sqrt{n} & -i\hbar v_F k_x & -E_n & 0 \\ i\hbar v_F k_x & -\hbar\omega\sqrt{n} & 0 & -E_n \end{bmatrix} = 0, \quad (18)$$

that the zeroth Landau level disperses as $E_0 = \pm\hbar v_F k_x$, which is same linear dispersion as for the B_z field.

For a magnetic field in the k_y-direction (B_y), we can rotate $H_{\rm Liu}$ around the [111]-axis in spin space in the different direction to get $H'''_{\rm Liu} = U_R^\dagger H'_{Liu} U_R = \hbar v_F \sigma_x (s_z k_x + s_x k_y) + \hbar v_F \sigma_y s_0 \, k_z$, which gives a result analogous to the B_x case: $E_0 = \pm\hbar v_F k_y$. This shows that the chiral zeroth Landau levels, and therefore also the CME, are expected to occur in every direction in $Bi_{1-x}Sb_x$.

APPENDIX B: LOCAL TRANSPORT

Hall bar samples have been fabricated to characterize the $Bi_{0.97}Sb_{0.03}$ flakes used for this work. The Hall bars were fabricated by using standard e-beam lithography, followed by sputter deposition of Nb with a capping layer of a few nm of Pd. Measurements were performed at T =10 K so as to not induce superconductivity in the $Bi_{0.97}Sb_{0.03}$ flake.

The longitudinal magnetoresistance, as shown in figure 2(a), exhibits a rather sharp angle dependence, with a negative magnetoresistance of about 12% for parallel electric and magnetic fields. Although subtle, Shubnikov-de Haas (SdH) oscillations can be observed. Figure 2(b) shows the SdH oscillations for perpendicular electric and magnetic fields, extracted by subtracting a simple smooth function from the measured data. The inset shows the obtained FFT spectrum, which reveals a single oscillation frequency $F \approx$17 T. The oscillation frequency shifts upon increasing the angle between the magnetic field and the c-axis of the crystal. Figure 2(c) shows the angle-dependence of this frequency, fitted with an ellipsoidal Fermi surface with an anisotropy of $k_z = 3.3 \cdot k_{x,y}$. This indicates that the oscillations originate from the bulk hole pocket [5].

APPENDIX C: CONSTANT LOCAL ELECTRIC FIELD

When studying the CME, in the ideal case one measures the non-local response of the chiral anomaly as a

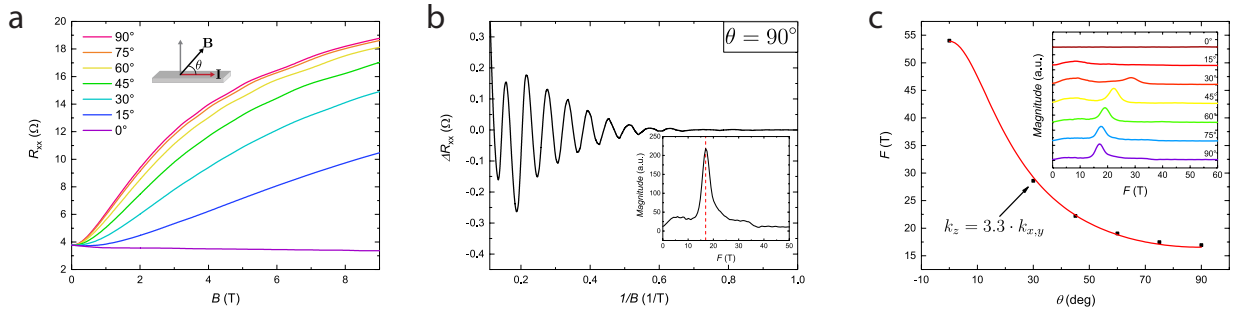

FIG. 2: **Local transport measurements on a Hall bar device**. **(a)** Longitudinal magnetoresistance for different angles θ between the applied magnetic field and the current direction. **(b)** Extracted Shubnikov-de Haas oscillations in the longitudinal resistance for the perpendicular field direction. The inset shows the FFT spectrum of the oscillations, with a clear peak at $F \approx 17$ T. **(c)** Oscillation frequencies from the Fourier transforms shown in the inset, as a function of the angle between the applied electric and magnetic fields. The fit to the data tells us that the oscillations originate from an elipsoidal Fermi surface with an anistropy of 3.3, which correpsonds to the bulk hole pocket.

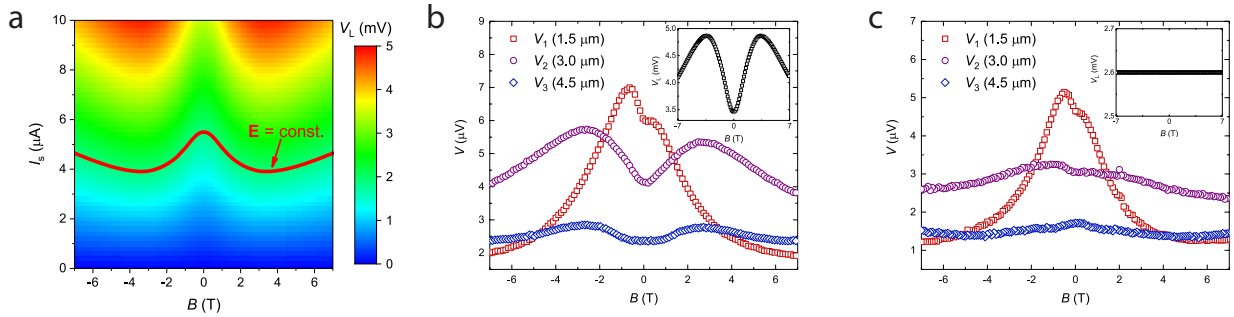

FIG. 3: **Extracting data for a constant electric field.** **(a)** Local voltage measured as a function of applied current and magnetic field. The red line corresponds to a constant local voltage for varying applied magnetic fields. **(b)** Measured non-local voltages when a constant current is applied at the source contacts and the local voltage changes with magnetic field as shown in the inset. **(c)** The extracted non-local data after following our method of retracing the red curve of panel (a) over each of the non-local voltage maps, thereby keeping the source voltage constant, as shown in the inset.

function of the applied magnetic field only, i.e. keeping the applied electric field at the source contacts constant. However, due to the low resistance of our sample, we can not voltage bias our sample and must resort to a current source, thereby causing the current to be constant as a function of the applied magnetic field. When measuring the local electric field, we find that this field is dependent on the magnetic field as well. Hence, sweeping the magnetic field changes both the strength of **E** and **B**, as follows directly from the chiral magnetic effect [6].

In order to obtain a data set with a constant electric field at the source contacts, we measured the local and non-local voltages as a function of both the applied current and magnetic field. The dependence of the local voltage on both parameters can be seen in figure 3(a). From this map, we can find a line for which $V_{\mathrm{L}}(I_s, B)$ is constant. This line is plotted on top of the map. By retracing the same line on the non-local voltage maps, we can extract the non-local voltages that correspond to the same constant local electric field and study the magnetic field dependence. In other words, we measure the local voltage $V_{\mathrm{L}}(I_s, B)$, extract the source current $I_s(V_{\mathrm{L}} = \mathrm{cst.}, B)$, and use this to find the non-local voltages for a constant local electric field: $V_{\mathrm{NL}}(I_s(B), B)$.

To increase the accuracy of the maps - we measured the field dependent data for 51 different values of the excitation current - we linearly interpolated our data as a function of I_s. Although recent work on $\mathrm{Bi}_{1-x}\mathrm{Sb}_x$ suggests that Ohm's law is violated in this system [7], our generated electric field is well above the non-linear regime.

Figure 3(b) shows the raw data, i.e. when we omit this procedure and would measure the voltages by applying a constant current. We clearly observe that the local voltage is not constant with respect to the magnetic field. Figure 3(c) shows the data when we follow our procedure. The local voltage is now constant as a function of the magnetic field and the large dips that were present in

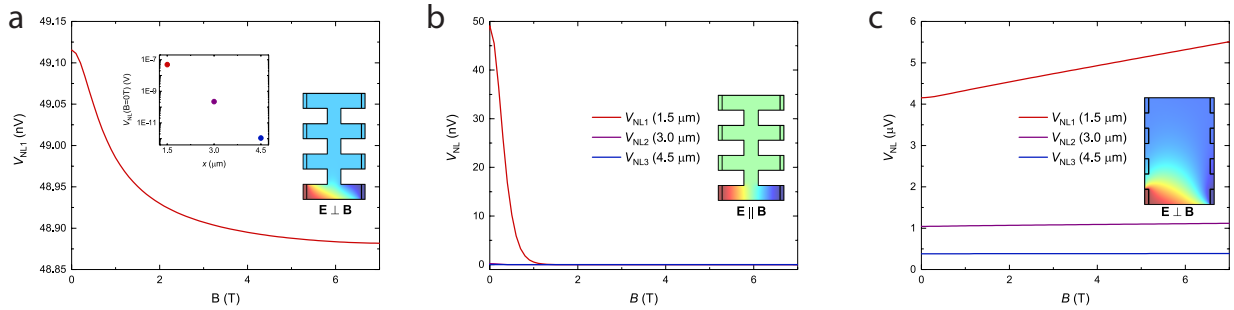

FIG. 4: **Simulation results for different geometries and/or field orientations.** For all panels, the device schematics show a contour plot of the voltage distribution for $B = 1$ T. **(a)** Simulation results for a structured device in perpendicular magnetic fields. A small negative magnetoresistance is found at the nearest voltage probe, while for the other probes the signal is completely negligible. **(b)** Same as panel (a), but for magnetic fields parallel to the source voltage. Current jetting causes a large negative magnetoresistance at the nearest contact, but this signal has vanished for further contacts. **(c)** Same as panel (a), but for a non-structured device (i.e. a flake) in perpendicular magnetic fields. The negative magnetoresistance from panel (a) is no longer present, indicating that the negative magnetoresistance in perpendicular fields is a geometrical effect.

figure 3(b) are less pronounced in figure 3(c).

APPENDIX D: MODELLING THE OHMIC CONTRIBUTION

The measured data comprises a combination of a chiral signal and a normal, i.e. Ohmic, contribution. To gain better insight in the Ohmic contribution, we modelled this contribution in COMSOL Multiphysics. The device geometry used for the measurements was replicated in COMSOL. One of the source leads was defined as a current source, sourcing 1 μA, while the other current lead was set as ground. The other terminals were voltage probes.

For simulations with perpendicular electric and magnetic fields (i.e. B in the z-direction and I in the x-direction), the three-dimensional conductivity tensor for a single band can be obtained from the Drude model [8];

$$\hat{\sigma_\perp} = \sigma_0 \begin{pmatrix} \frac{1}{1+(\mu B)^2} & \frac{\mu B}{1+(\mu B)^2} & 0 \\ -\frac{\mu B}{1+(\mu B)^2} & \frac{1}{1+(\mu B)^2} & 0 \\ 0 & 0 & 1 \end{pmatrix}, \tag{19}$$

where $\sigma_0 = ne\mu$. For parallel electric and magnetic fields (i.e. B in the x-direction), one can show that the conductivity tensor is given by

$$\hat{\sigma_\parallel} = \sigma_0 \begin{pmatrix} 1 & 0 & 0 \\ 0 & \frac{1}{1+(\mu B)^2} & \frac{\mu B}{1+(\mu B)^2} \\ 0 & -\frac{\mu B}{1+(\mu B)^2} & \frac{1}{1+(\mu B)^2} \end{pmatrix}. \tag{20}$$

Upon changing the tensor in COMSOL we effectively rotate the magnetic field with respect to the sample. Figure 4 shows the results of simulations for different structures (depicted as insets within the figures) and different orientations of the magnetic field with respect to the electric field. For every simulation we used a carrier density of $n = 4 \cdot 10^{17}$ m^{-2} and mobility $\mu = 2$ m^2/Vs.

Figure 4(a) shows the simulation results for a magnetic field perpendicular to the plane (and thus to the current). The sample is shaped into a non-local structure with a geometry as used in the experiments. We observe decreasing non-local voltages at the nearest contact with increasing perpendicular magnetic field. As the used model only captures the Drude conductivity, the observed decrease cannot be explained by a chiral component. The contacts further away from the source all returned negigibly small voltages.

Figure 4(b) shows the non-local voltages for magnetic fields parallel to the electric source field. The strongly decreasing magnetoresistance can be explained by an effect called current jetting. Current jetting, as follows from the conductivity tensor for parallel fields, is an effect where the magnetic field suppresses current flow in the transverse direction [9–11]. This reduces the amount of current that spreads out towards the non-local voltage probes, resulting in a decrease in the voltages that are measured. The fact that current jetting can also introduce negative magnetoresistance, is (among other effects) one of the main reasons that observing negative magnetoresistance itself is not a proof of observing the chiral anomaly. However, the simulated non-local voltages decrease (even vanish) much faster than observed in experiments. From this, we conclude that the negative magnetoresistance in our samples is not caused by current jetting.

In panel (a), we observed a decreasing non-local voltage while the electric and magnetic fields were perpendicular to each other. To further investigate the nature of this decrease, simulations were performed on a rect-

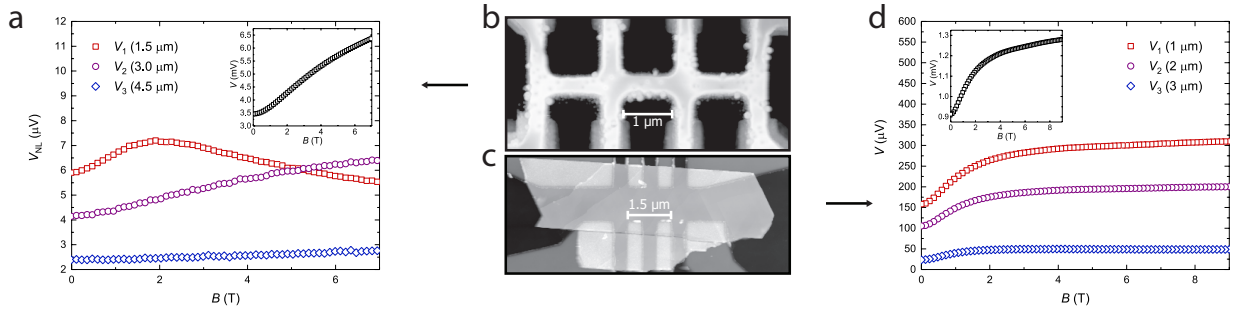

FIG. 5: **Measurement data for perpendicular electric and magnetic fields.** For all transport measurements in this figure, data has been measured for constant source current. **(a)** Magnetoresistance data measured for the non-local device of the main text, in perpendicular magnetic fields. Inset: voltage at the source contacts. **(b)** AFM image of the structured non-local sample as shown in the main text, but presented again for the ease of comparison. **(c)** AFM image of a non-local sample for which the flake has not been etched into a channelled structure. **(d)** Same as panel (a), but for the unstructured device.

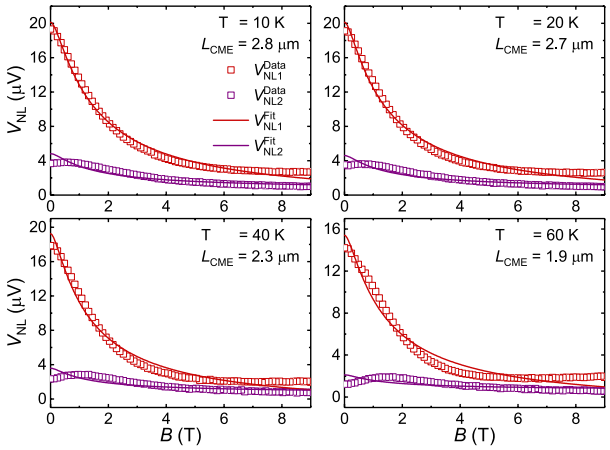

FIG. 6: **Fitting the intervalley diffusion length for different temperatures.** Examples of fits to the data in order to extract the chiral contribution (see main text) and Ohmic contribution (which is constant) simultaneously for the different temperatures.

angular, unstructured flake with 8 contacts, as shown in figure. 4(c). The non-local voltages now show an upturn with increasing parallel magnetic field. By comparing panels (a) and (c), which make use of the same conductivity tensor and only differ in terms of geometry, we conclude that the decreasing non-local voltage in panel (a) is caused by the geometry of the device.

APPENDIX E: NON-LOCAL MEASUREMENTS AT PERPENDICULAR ELECTRIC AND MAGNETIC FIELDS

Measurements have been performed for perpendicular electric and magnetic fields. In figure 5 we present the data for two different samples. Striking is that for panel (a) we observe a decrease of V_1 as a function of magnetic field, while in the panel (d) we only observe the standard upturn with magnetic field, similar to the data measured for the Hall bar sample.

In the simulations of the previous section, we found that this negative magnetoresistance in perpendicular fields is a geometrical effect. Comparing panels (a) and (b) of figure 5 to panel (a) of the simulations (figure 4), and panels (c) and (d) of figure 5 to panel (c) of the simulations, we see that the experimental data confirms this. That the simulations are much more distinctive on the two different geometries, is because of the simulation taking only a single band into account for the conductivity, while in reality the conductivity is mediated by four channels. Furthermore, as can be seen from panel (c), the flakes are not always uniform in thickness and are not as well defined as the geometries in our simulations.

APPENDIX F: TEMPERATURE DEPENDENCE OF THE CHIRAL DIFFUSION LENGTH

The device used in the main text to study the temperature dependence had one broken voltage probe. As a consequence, only 2 non-local voltages were measured. This device has contacts spaced 1.5 μm apart, with twice this spacing in the middle, so that the contacts $V_{\mathrm{NL}1,2}$ are located at 3.0 μm and 7.5 μm respectively.

The measurements for this device were performed using a single, constant current. Because of the linearity of the measured voltage as a function of the applied current (see section C), we can still extrapolate the data by using the recorded data point and the fact that $V_L(I_s = 0) = 0$ V. Then, the procedure as outlined in section C was followed to convert the mapped data into data for which the local electric field is effectively con-

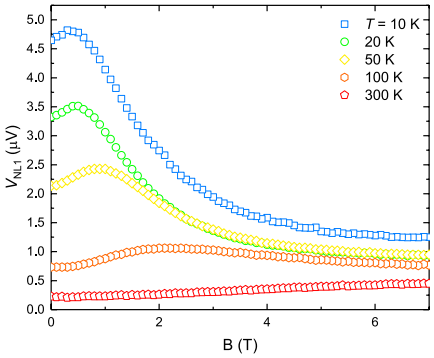

FIG. 7: **Temperature dependence of the smaller non-local device described in the main text.** The temperature dependence of the nearest non-local contact shows the same general trend as the device used for the temperature-dependence in the main text.

stant. In figure 6 we present some examples of fits to the data to extract the temperature-dependent chiral diffusion length as presented in the main text. As described in the main text, all fits were performed on the intermediate field data (2 T-5.5 T).

Lastly, figure 7 shows the temperature dependence of the non-local voltage of the smallest sample shown in the main text. Here, we also observe a decreasing strength of the anomaly with increasing temperature. The observed peak in the curve drifts to higher magnetic fields with temperature. For temperatures above 100 K, we do not observe negative magnetoresistance.

* These two authors contributed equally.

[1] B.J. Yang N. Nagaosa, Nat. Commun. **5**, 4898 (2014)
[2] A.A. Zyuzin and A.A. Burkov Phys. Rev. B **86**, 115133 (2012)
[3] C.X. Liu, X.L. Qi, H. Zhang, X Dai, Z Fang, S.C. Zhang Phys. Rev. B **82**, 045122 (2010)
[4] J.C.Y. Teo, L. Fu, C.L. Kane Phys. Rev. B **78**, 045426 (2008)
[5] C. Li, J.C. de Boer, B. de Ronde, S.V. Ramankutty, E. van Heumen, Y. Huang, A. de Visser, A.A. Golubov, M.S. Golden, A. Brinkman, Nat. Mater. **17**, 875880 (2018)
[6] Q. Li, D.E. Kharzeev, C. Zhang, Y. Huang, I. Pletikosi, A.V. Fedorov, R.D. Zhong, J.A. Schneeloch, G.D. Gu, T. Valla, Nat. Phys. **12**, 550554 (2016)
[7] D. Shin, Y. Lee, M. Sasaki, Y.H. Jeong, F. Weickert, J.B. Betts, H.J. Kim, K.S. Kim, J. Kim Nat. Mater. **16**, 10961099 (2017).
[8] S. Datta, Electronic Transport in Mesoscopic Systems, Cambridge University Press (1995)
[9] A.B. Pippard, Magnetoresistance in metals, Cambridge University Press (1989).
[10] , M. Hirschberger, S. Kushwaha, Z. Wang, Q. Gibson, S. Liang, C.A. Belvin, B.A. Bernevig, R.J. Cava, N.P. Ong, Nat. Mater. **15**, 11611165 (2016)
[11] R.D. dos Reis, M.O Ajeesh, N. Kumar, F. Arnold, C. Shekhar, M. Naumann, M. Schmidt, M. Nicklas, E. Hassinger, New Journ. of Phys. **18** (2016)
[12] S.A. Parameswaran, T. Grover, D.A. Abanin, D.A. Pesin, A. Vishwanath, Phys. Rev. X **4**, 031035 (2014)
[13] C. Zhang, E. Zhang, W. Wang, Y. Liu, Z.G. Chen, S. Lu, S. Liang, J. Cao, X. Yuan, L. Tang, Q. Li, C. Zhou, T. Gu, Y. Wu, J. Zou, F, Xiu, Nat. Commun. **8**, 13741 (2017)
[14] S. Liang, J. Lin, S. Kushwaha, J. Xing, N. Ni, R.J. Cava, N.P. Ong, Phys. Rev. X **8**, 031002 (2018)